Phase-Field Modeling of Vapor Bubble Growth in a Microchannel

R. Jafari and T. Okutucu-Özyurt*
Department of Mechanical Engineering, Middle East Technical University, Dumlupınar Blv. No: 1, 06800 Ankara, Turkey

Received: 30 November 2014, Accepted: 5 May 2015

ABSTRACT

A numerical model based on Cahn–Hilliard phase-field method is introduced for the first time in the literature to investigate the hydrodynamics and heat transfer characteristics of a vaporized elongated bubble in a rectangular microchannel. In the simulations, the initially nucleated bubble starts growing as it comes in contact with superheated water. The effects of the water inlet velocity and the bubble contact angle on the temporal evolution of the average heat transfer coefficient are also reported. Both qualitative and quantitative comparisons indicated that the numerically obtained bubble shape and the growth rate are in very good agreement with the experimental results available in the literature.

NOMENCLATURE

C_p	specific heat capacity, [J/kg·K]
f_{mix}	mixing energy, [N]
$\boldsymbol{F}$	surface tension force per unit volume, [N/m^3]
$\boldsymbol{g}$	gravity acceleration vector, [m/s^2]
G	chemical potential, [Pa]
H_{lg}	latent heat, [J/kg]
k	thermal conductivity, [W/m·K]
$\dot{m}$	mass rate of evaporation, [kg/m^2·s]
p	pressure, [Pa]
r	constant, [m/s]
R	constant, [m/s]
t	time, [s]
T	temperature, [K]
$\boldsymbol{u}$	velocity vector, [m/s]
V_f	volume fraction
γ	mobility, [m^3.s/kg]
δ	smoothed representation of the interface, [1/m]
$\in$	capillary width, [m]
λ	mixing energy density, [N]
μ	viscosity, [Pa·s]
ρ	density [kg/m^3]
σ	surface tension coefficient [N/m]
ϕ	phase field variable
ψ	secondary phase field variable

Subscripts

L	Liquid
Sat	Saturation
V	Vapor

*Corresponding author: E-mail: okutucu@metu.edu.tr

1. INTRODUCTION

Thermal management of microelectronic devices with reduced size and increased functionality has become more challenging due to high heat fluxes localized in small volumes. Flow boiling through microchannels has been extensively studied as a cooling alternative because of its capability of providing a high heat transfer rate. Some recent investigations on flow pattern and heat transfer during flow boiling in microchannels have been reported in a few review articles [1-5].

Vaporized bubble of microscopic size in a microchannel grows rapidly and fills the entire cross section of the microchannel in milliseconds, and eventually, an elongated bubble or slug flow appears in the microchannel. Moreover, at the microscale, the surface tension and evaporation momentum forces are the dominant forces controlling the bubble dynamics [6]. Accordingly, the models and correlations developed for macroscale boiling heat transfer may not be applicable for microscale two phase flows. Furthermore, the experimental efforts are limited due to the small scales, while multiphase CFD techniques are emerging as powerful tools to investigate the fluid dynamics and the heat transfer at such scales.

Zu et al. [7] performed a 3-D numerical simulation of bubble formation using the volume of fluid (VOF) method in the commercial CFD software ANSYS FLUENT. In the mentioned study, the bubble generation and growth was simulated based on the concept of pseudo-boiling in which the bubble is generated by the injection of vapor from a hole through the heated side wall of the channel. The hole serves as a nucleation site, and the bubble growth is then driven by a constant heat flux.

Dong et al. [8] investigated the effect of bubble nucleation, growth and departure on fluid flow and heat transfer in a microchannel via 2-D Lattice Boltzmann modeling. A single seed bubble, a cavity, two cavities, one seed bubble and a reentrant cavity were simulated in a microchannel with dimensions of 0.2mm×5.3mm.

Sun et al. [9] proposed a vapor-liquid phase model in ANSYS FLUENT which considers both superheated and saturated phases. The vapor near the wall gets heated and becomes superheated, which drives the mass transfer at the interface. The vapor stays motionless while the saturated liquid and the interface are driven away from the wall. Magnini et al. [10] implemented ANSYS FLUENT to investigate in detail the bubble dynamics and the wall heat transfer of flow boiling in a circular microchannel of diameter 0.5 mm using a 2-D axisymmetric formulation. Different refrigerants, namely, R113, R134a and R245fa were investigated with two different saturation temperatures of 31°C and 50°C. The bubble nose acceleration to downstream was in good agreement with a theoretical model [11].

Mukherjee et al. [12] studied a vapor bubble growing on a heated wall inside a microchannel with a hydraulic diameter of 229 μm. They solved the continuity, Navier- Stokes and energy equations using the SIMPLER algorithm. Firstly, the water bubble growth rate and the bubble shape were validated by experimental results. Then a parametric numerical study was carried out to analyze the effects of the wall superheat, the inlet liquid flow rate, the surface tension and the contact angle on the bubble growth rate inside the microchannel.

Jafari and Okutucu [13] studied numerically the bubble dynamics and heat transfer during nucleate boiling in a micrtube with the diameter of 200 μm using the Arbitrary Lagrangian-Eulerian method (ALE). The Navier-stokes equations have been solved in a domain as a single flow with two subdomains and a moving mesh at the interface of the liquid and vapor phases.

Zhou et al. [14] used the level set two-phase flow model to simulate the nucleate boiling in microchannels. The model for the bubbles in uniformly superheated liquid, and flow boiling regime were identified and validated. Reentrant cavities were formed along the microchannel to compare the performances of the enhanced and plain-wall microchannels. The results demonstrated facilitated nucleation and enhanced critical heat flux. The reentrants were optimized based on which nucleates first under a given set of conditions of rather low superheating.

Akhlaghi Amiri and Hamouda [15] compared the accuracy and running time of two-phase flow through porous media by 2-D modeling with conservative level set method (LSM) and Cahn–Hilliard phase-field method (PFM) in COMSOL Multiphysics. It was concluded that the PFM is more successful in capturing physical details. Furthermore, the PFM results, such as, the pressure gradients and the flow profiles in the media were more realistic than those for the LSM and it took less running time for the PFM method. Besides, the LSM needed a thinner interface for convergence compared to the PFM and was unsuccessful in the volume conservation and no slip boundary conditions.

The objective of the present study is to employ the phase-field model to investigate the hydrodynamics and heat transfer characteristics of two-phase flow during nucleate boiling in microchannels. An extended phase-field method has been used, for the first time in literature, to simulate a nucleated vapor bubble growing inside a heated microchannel.

2. NUMERICAL METHOD

2.1. Phase-Field Method

The interface of two immiscible fluids often needs special consideration. One method of handling moving boundaries is to keep track of the motion of material points residing on the interface. Numerically, this may be realized by using grid points moving either with the local fluid velocity or a mesh velocity. This Lagrangian approach is often known as interface tracking. However, interfacial deformation causes some difficulties as remeshing and interpolation increasing the computational cost and error. An alternative to interface tracking is to track the fluid flow of both components on a fixed Eulerian grid, with the interface being determined or reconstructed at each time step by using a scalar indicator function. Examples of this class of methods are the volume of fluid (VOF) method, the level-set method (LS) and the phase-field method [16]. The diffuse interface models for a wide variety of interfacial phenomena such as binary fluids are addressed in literature [17-19]. The interface topology is estimated poorly by the volume of fluid approach used to calculate the surface tension force [13]. The phase-field method not only convects the fluid interface as in the level set method, but it also ensures that the total energy of the system diminishes correctly.

The phase-field based models replace sharp fluid-material interfaces by thin but nonzero thickness transition regions in which the interfacial forces are smoothly distributed [20]. The phase-field method has been broadly used in physics, material science [21], fracture mechanics [22] and multiphase flow [23,24]. The basic idea is to introduce an order parameter or phase-field that varies continuously over thin interfacial layers and is mostly uniform in the bulk phases. The order parameter has a physical meaning, and can be applied to different phase change phenomena by a proper modification of the free energy. An extremely thin interface layer is required to properly model the physics of the problem. In addition, relatively high computational resolution is required to handle the large gradients at the interface [25].

The interface has a small but finite thickness which contains two mixed components (phases), and stores a mixing energy. The free energy density of an isothermal mixture of two immiscible fluids is the sum of the mixing energy and the elastic energy. The mixing energy may be expressed as [19]

$$f_{mix}\left(\phi,\nabla\phi\right)=\frac{1}{2}\lambda\left|\nabla\phi\right|^2+\frac{\lambda}{4\epsilon^2}(\phi^2-1)^2 \tag{1}$$

where ϕ is the dimensionless phase-field variable defined such that the volume fraction of the components of the fluid are $(1+\phi)/2$ and $(1-\phi)/2$. The quantity λ [N] is the mixing energy density, and ϵ [m] is a capillary width that scales with the thickness of the interface.

The evolution of the phase-field variable ϕ is governed by the Cahn-Hilliard equation, which is a 4th-order partial differential equation in the form

$$\frac{\partial\phi}{\partial t}+\boldsymbol{u}\sum\nabla\phi=\nabla\sum\gamma\nabla G \tag{2}$$

where $\boldsymbol{u}$ and γ are the velocity vector [m/s] and the mobility [m^3·s/kg], respectively, and G [Pa] is the chemical potential which is defined as

$$G=\lambda\left[-\nabla^2\phi+\frac{\phi(\phi^2-1)}{\epsilon^2}\right] \tag{3}$$

The mixing energy density, λ, and the capillary width, ϵ, are related to the surface tension

coefficient, σ [N/m], through Eqn.(4) [19].

$$\sigma = \frac{2\sqrt{2}}{3}\frac{\lambda}{\epsilon} \tag{4}$$

The interface thickness is assumed to be the half of the mesh element size at the interface. Then the capillary width, and consequently, the mixing energy density may be found using Eqn. (4). For instance, if the mesh size at the interface is 0.8 μm, the capillary width will be ϵ = 0.4 μm and for water with a surface tension of σ = 0.0588 N/m, the mixing energy density will be $\lambda = 0.25\times10^{-6}$ N.

The Cahn-Hilliard equation forces ϕ to take a value of 1 or –1 except in a very thin region at the fluid-fluid interface.

The phase-field interface decomposes Eqn. (2) into two second-order partial differential equations as

$$\frac{\partial\phi}{\partial t} + \boldsymbol{u}\sum\nabla\phi = \nabla\sum\frac{\gamma\lambda}{\epsilon^2}\nabla\psi \tag{5}$$

$$\psi = -\nabla\sum\epsilon^2\nabla\phi + (\phi^2 - 1)\phi \tag{6}$$

where ψ is the phase-field help variable.

2.2. Domain Equations

Generally, the well-known Navier-Stokes equations describe the velocity and pressure fields for the liquid phase as follows

$$\rho_L\frac{\partial\boldsymbol{u_L}}{\partial t} + \rho_L\left(\boldsymbol{u_L}\cdot\nabla\right)\boldsymbol{u_L} = \nabla\cdot\left[-p_L\mathbf{I} + \mu_L\left(\nabla\boldsymbol{u_L} + \left(\nabla\boldsymbol{u_L}\right)^T\right)\right] + \rho_L\boldsymbol{g} + \boldsymbol{F} \tag{7}$$

$$\nabla\cdot\boldsymbol{u_L} = 0 \tag{8}$$

where L and V denote the liquid and vapor phases, respectively. $\boldsymbol{g}$ [m/s^2], $\boldsymbol{F}$ [N/m^3], p [Pa] and μ[Pa·s] are the gravitational acceleration vector, the surface tension force per unit volume, the pressure and the viscosity, respectively.

For the vapor phase, the following weakly compressible Navier-Stokes equations are solved.

$$\rho_V\frac{\partial\boldsymbol{u_V}}{\partial t} + \rho_V\left(\boldsymbol{u_V}\cdot\nabla\right)\boldsymbol{u_V} = \nabla\cdot\left[-p_V\mathbf{I} + \mu_V\left(\nabla\boldsymbol{u_V} + \left(\nabla\boldsymbol{u_V}\right)^T\right) - \frac{2}{3}\mu_V\left(\nabla\cdot\boldsymbol{u_V}\right)\boldsymbol{I}\right] + \rho_V\boldsymbol{g} + \boldsymbol{F} \tag{9}$$

$$\frac{\partial\rho_V}{\partial t} + \nabla\cdot\left(\rho_V\boldsymbol{u}_V\right) = 0 \tag{10}$$

The vapor density is determined through the ideal gas law.

Since the temperature at the liquid-vapor interface is set to the saturation temperature, a constant temperature throughout the entire vapor is obtained by solving the conservation of energy equation which, in this case, is the heat conduction equation.

$$\rho C_P\frac{\partial T}{\partial t} + \rho C_P\left(\boldsymbol{u}\cdot\nabla\right)T = \nabla\cdot K\nabla T_V \tag{11}$$

In this equation, C_p [J/kg·K] and K [W/m·K] are the specific heat and the thermal conductivity, respectively.

2.3. Evaporation Model

To investigate the evolution of the interface as well as the bulk fluid, the phase-field method is coupled with the foregoing conservation equations for the mass, momentum and energy. For this reason, the use of any special algorithm for tracking the interface or satisfying the sharp interface balances is not required.

The Cahn-Hilliard Eqn. (2) for the phase-field variable is modified to include the phase change as

$$\frac{\partial \phi}{\partial t} + \boldsymbol{u} \cdot \nabla \phi - \dot{m}\delta\left(\frac{V_{f,V}}{\rho_V} + \frac{V_{f,L}}{\rho_L}\right) = \nabla \cdot \frac{\gamma\lambda}{\epsilon^2} \nabla \psi \tag{12}$$

where $V_{f,L}$ and $V_{f,V}$ are the volume fractions of the liquid and the vapor, respectively.

The quantity δ [1/m] is a smoothed representation of the interface between the two phases. It is defined as

$$\delta = 6V_{f,L}(1 - V_{f,L})\frac{|\nabla \phi|}{2} \tag{13}$$

The surface tension force appears as a volumetric body force in the momentum equation (7) as

$$\rho \frac{\partial \boldsymbol{u}}{\partial t} + \rho\left(\boldsymbol{u} \cdot \nabla\right)\boldsymbol{u} = \nabla \cdot \left[-p\boldsymbol{I} + \mu\left(\nabla \boldsymbol{u} + \left(\nabla \boldsymbol{u}\right)^T\right)\right] + \rho \boldsymbol{g} + G\nabla \phi \tag{14}$$

The continuity equation (10) is also modified to include the effect of the phase change from liquid to vapor [26]

$$\nabla \cdot \boldsymbol{u} = \dot{m}\delta\left(\frac{1}{\rho_V} - \frac{1}{\rho_L}\right) \tag{15}$$

The mass flux leaving the interface can be evaluated from the conductive heat flux as

$$\dot{m} = -\frac{k_V \nabla T}{h_{lg}} \tag{16}$$

Due to the large differences in the thermophysical properties across the interface, a more suitable correlation for the evaporation rate may be of the form

$$\dot{m} = rV_{f,L}\rho_L \frac{T - T_{sat}}{T_{sat}} \tag{17}$$

where r is a constant which is set equal to 0.1 by Lee [27] and 100 by Yang et al. [28]. In the present study, $V_{f,L}$ is included in Eqn. (13) for δ, and the evaporation mass flux is calculated as

$$\dot{m} = R\rho_L \frac{T - T_{sat}}{T_{sat}} \tag{18}$$

where R [m/s] is a constant , and should be sufficiently large to keep the interface at the saturation temperature. In this study, the results numerically diverge for R values greater than 0.2. In addition, R values less than 0.06 yield an increased deviation of the interface temperature from the saturation

temperature. The value of R is set to 0.1 m/s which is optimized based on the minimization of the error between the experimental data [12] and the simulations.

The mass flux is added in the energy equation (11) to include the effect of the generated latent heat at the interface as

$$\rho C_P \frac{\partial T}{\partial t} + \rho C_P \left(\boldsymbol{u} \cdot \nabla \right) T = \nabla \cdot \mathrm{k} \nabla T - \dot{m} \delta h_{lg} \tag{19}$$

where h_{lg} [J/kg] is the latent heat. The thermal conductivity and the specific heat are calculated as functions of the volume fraction of the two phases as follows

$$k = \left(k_L - k_V \right) V_{f,L} + k_V \tag{20}$$

$$C_p = \left(C_{p,L} - C_{p,V} \right) V_{f,L} + C_{p,V} \tag{21}$$

2.4. Validation of the Model

The growing rate and the shape of the vapor bubble inside the microchannel have been validated by the experimental data of Mukherjee et al. [12] for a microchannel of 229 μm hydraulic diameter. The temperatures of the side walls and the bottom wall are set to 102.1°C. The top wall is adiabatic. Water flows through the microchannel with Reynolds number Re = 100 at saturation temperature. The contact angle at the walls is $\theta = 30°$. Initially it is presumed that a nucleated bubble of 40 μm diameter exists inside the microchannel on the bottom wall with its center located at x = 0, y = 229 μm, and z = 20 μm as shown in Figure 1. The simulations have been performed by the help of the finite element software COMSOL Multiphysics™ along with the described modifications in the continuity, momentum and energy equations to account for the phase change. The mesh convergence analysis, and the vapor bubble growth rate and shape are presented next.

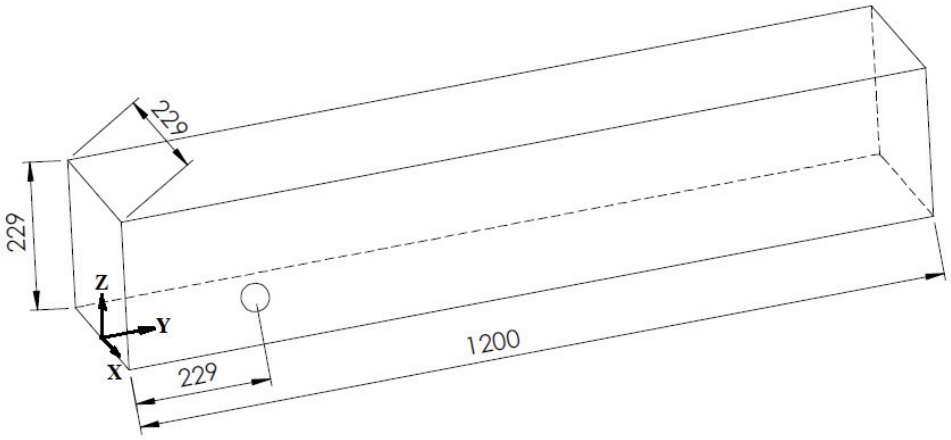

Figure 1. The computational domain (the unit of the dimensions is μm).

2.4.1. Mesh Convergence Analysis

At the thin interface, high gradients of the investigated parameters exist. For this reason, finer grids are required at the interface compared to the remaining regions of the model. Figure 2 shows the distribution of the grids inside and around the bubble for the initialization of the simulations. The interface thickness is adjusted as half of the mesh element size in the region where the interface passes. Different triangular mesh sizes are used to calculate the bubble growth rate for the optimization of the numerical accuracy and the computational time. With an Intel® Xeon® CPU E5-16200 @ 3.60 GHz processor with 32 GB RAM, the computation times were about 40, 681 and

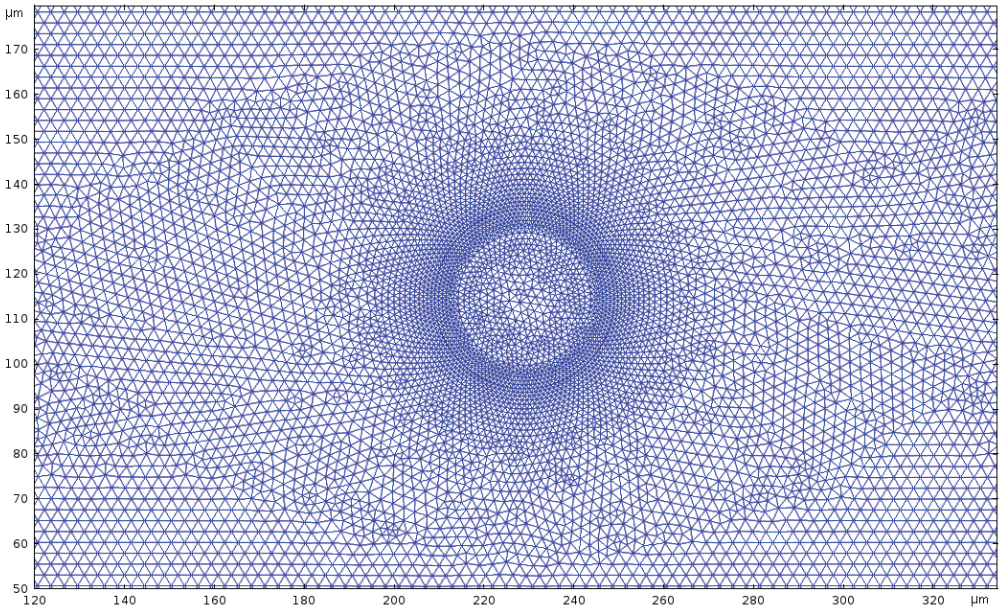

Figure 2. The close up view of the computational mesh inside and around the initial bubble.

7326 minutes, for coarse grids (18682), fine grids (88814) and finer grids (355256), respectively. Figure 3 illustrates the equivalent diameter of the bubble for the three different grid sizes at various time steps. With the two finer meshes, about 0.07 ms time difference occurred for the bubble to grow to a diameter of 0.2 mm, and a maximum difference of 4.2% has been observed between the bubble diameters obtained at the same instant. The difference in the bubble diameter has reached 26.4% for the two coarser meshes. Hence, the simulations have been continued with 88814 meshes. At the interface between the liquid and vapor domains, the mesh sizes vary between 0.03 µm to 1 µm. The mesh size grows up to 2.9 µm far from the interface.

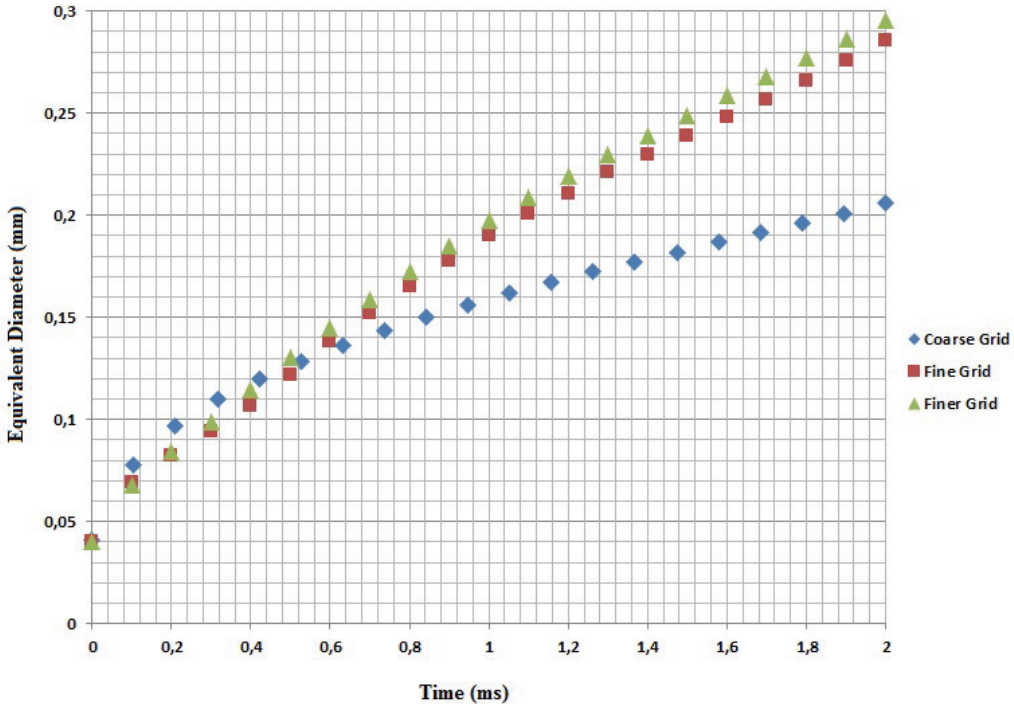

Figure 3. Equivalent diameter of the bubble with three different grid sizes

2.4.2. Vapor Bubble Growth Rate and Shape

The simulations have been performed in a two dimensional (2D) domain to save computational power and time. The gravitational force is employed along the side plane (in z-direction). The equivalent diameter of the nucleated vapor bubble is calculated along the top plane (the central horizontal XY plane) and the side plane (the central vertical ZY plane) of the microchannel. Figure 4 quantitatively compares the bubble growth rates obtained by the present simulations and available experimental data [12]. As may be observed from Figure 4, the results of the simulation are in very good agreement with the experimental data. In addition, the temporal evolution of the bubble shape is qualitatively compared with the same experimental study [12] as illustrated in Figure 5. There are deviations in the growth rate and the shape of the bubble from those of the experimental study with increase in time. The maximum deviation is 18%. To investigate the reasons for the deviations, the total free energy of the system has been calculated using the surface tension (Eqn. (22)), as well as the mixing energy (Eqn. (23)) [16].

$$F_1 = \int \sigma dA \tag{22}$$

$$F_2 = \int \left(\frac{1}{2}\lambda\left|\nabla\phi\right|^2 + \frac{\lambda}{4\varepsilon^2}(\phi^2-1)^2\right)dV \tag{23}$$

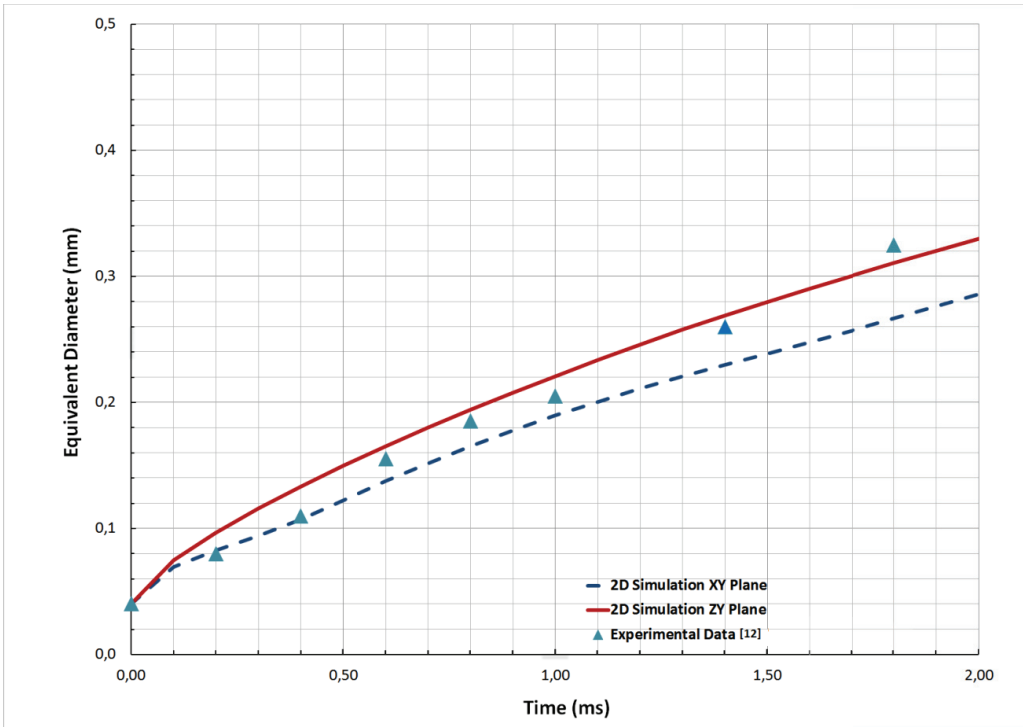

Figure 4. The comparison of the bubble growth rates of the present numerical simulation and the experimental data [12].

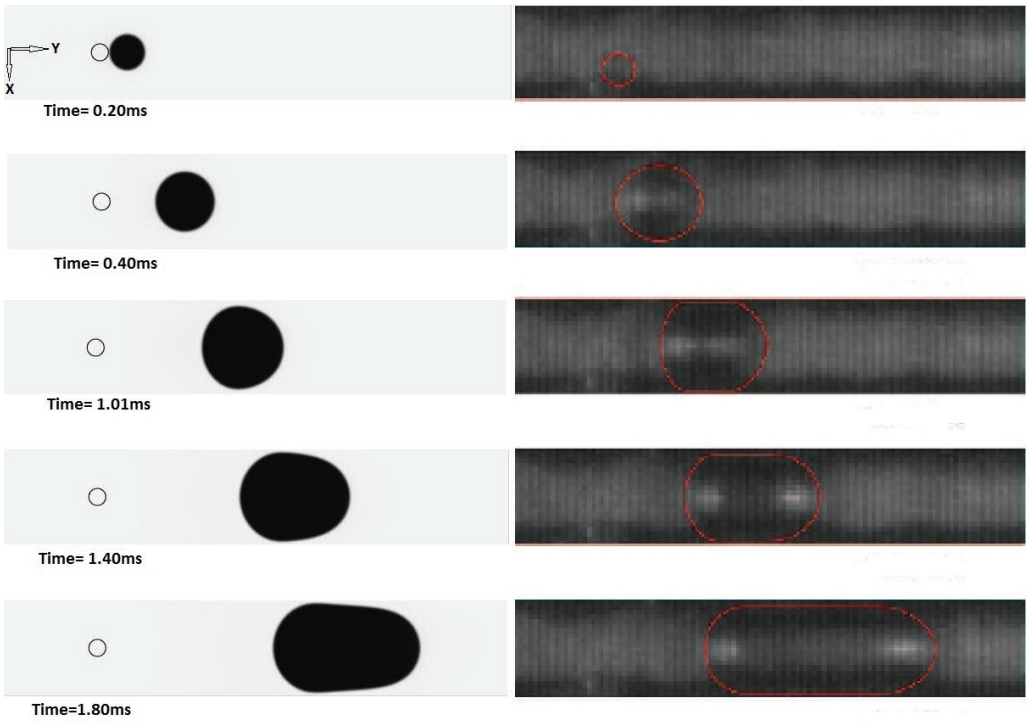

Figure 5. The comparison of the bubble shapes of the present numerical study (left) and the experimental study [12] (right), at the same instant.

Figure 6 indicates the difference, which may be attributed to the mass losses that occur during the bubble growth with increasing time.

In the simulations, a non-conservative form of the phase-field, which is an approximate solution to Eqn. (12), has been employed. The non-conservative solution form is better suited for numerical calculations, and converges without difficulty.

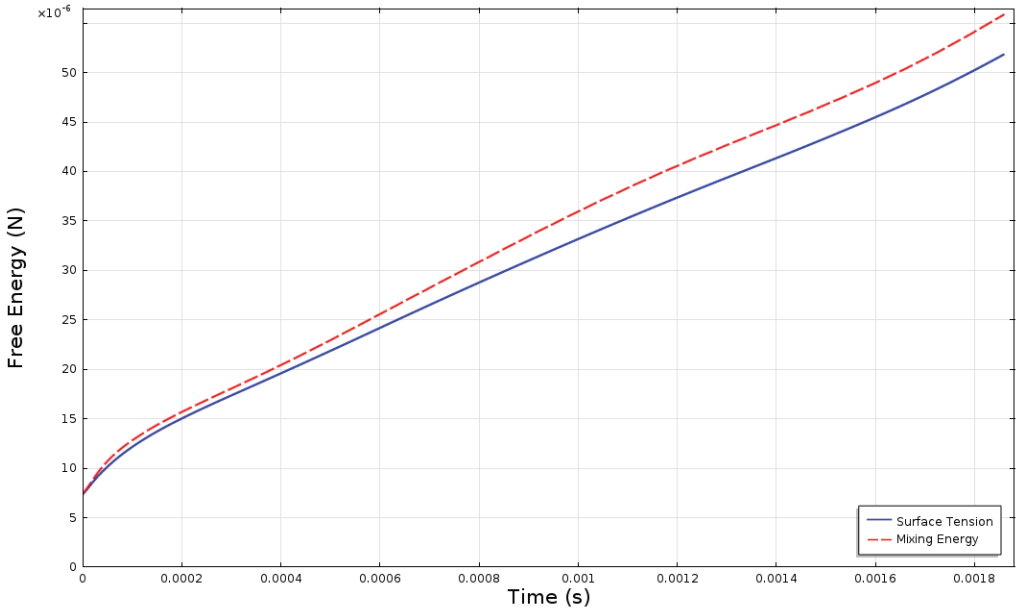

Figure 6. The surface tension and mixing energy inside the bubble interface.

3. RESULTS AND DISCUSSION

3.1. Flow and Temperature Field around the Bubble

For analyzing the local hydrodynamics and heat transfer of the vapor bubble inside the microchannel in detail, the water inlet and initial temperatures and the wall temperature are set to 102.1°C. This way, the effect of convective heat transfer between the wall and water has been eliminated. Only the boiling heat transfer effect is maintained. Figures 7a, b depict the velocity distribution inside and around the elongated bubble in the central horizontal XY plane and the central vertical ZY plane, respectively. Both distributions were captured at time t = 1.8 ms.

Figure 7a shows that the downstream velocity increases up to 0.54 m/s whereas the upstream velocity remains low at about 0.13 m/s. It may be inferred that the liquid is pushed forward at a faster rate downstream due to the bubble growth. The high rate of evaporation at the nose of the bubble, which is indicated by the greater velocities around the interface, accelerates the bubble nose movement. As a result, and based on the conservation of mass, the velocity of the vapor inside the bubble increases up to 0.8 m/s near the nose. It can also be observed that the thin liquid film between the wetted walls and the bubble downstream has higher velocity which increases the rate of evaporation.

Figure 7b illustrates higher velocity downstream compared to the upstream of the bubble. The downstream velocity is 0.58 m/s while the upstream velocity is about 0.13 m/s. A high rate of evaporation is indicated in the regions of high velocity gradients, namely, the bubble nose, and the liquid film between the bottom wall and the bubble nose. Since the top wall is adiabatic, there is no heat flux from the top wall into to the microchannel. Hence, the evaporation rate at the top of the bubble is lower.

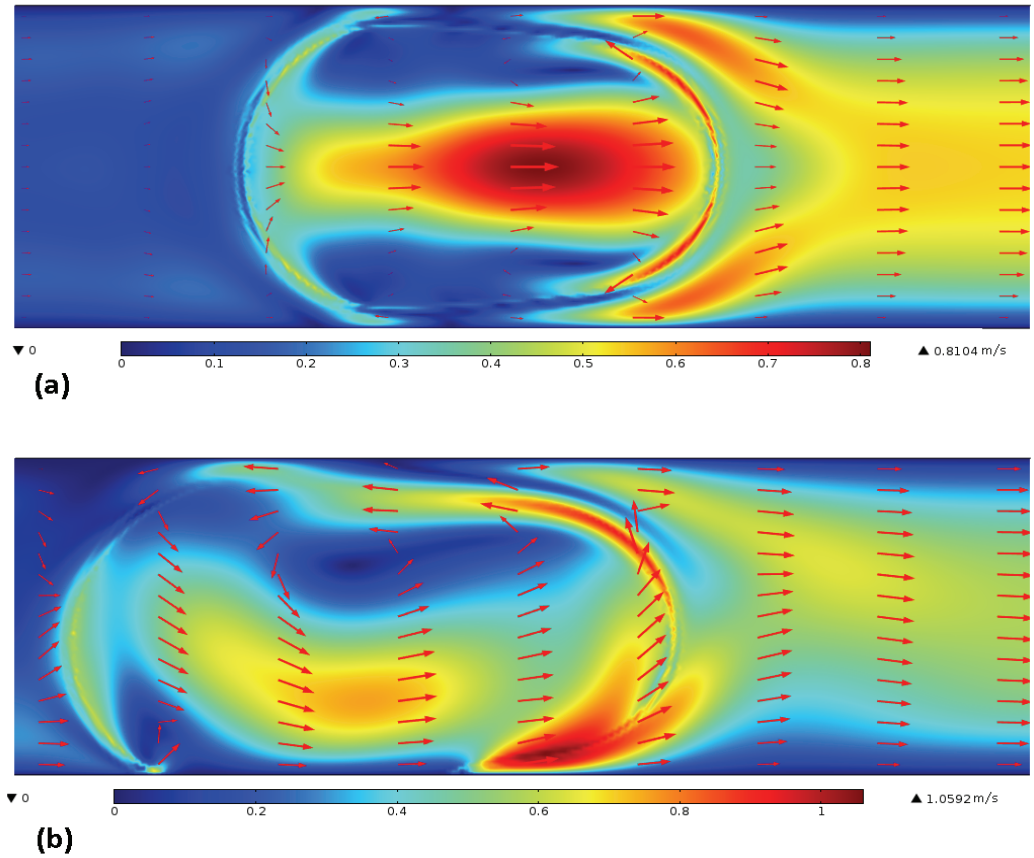

Figure 7. The velocity distribution inside and around the elongated vapor bubble (a) XY plane and (b) ZY plane at t = 1.8 ms.

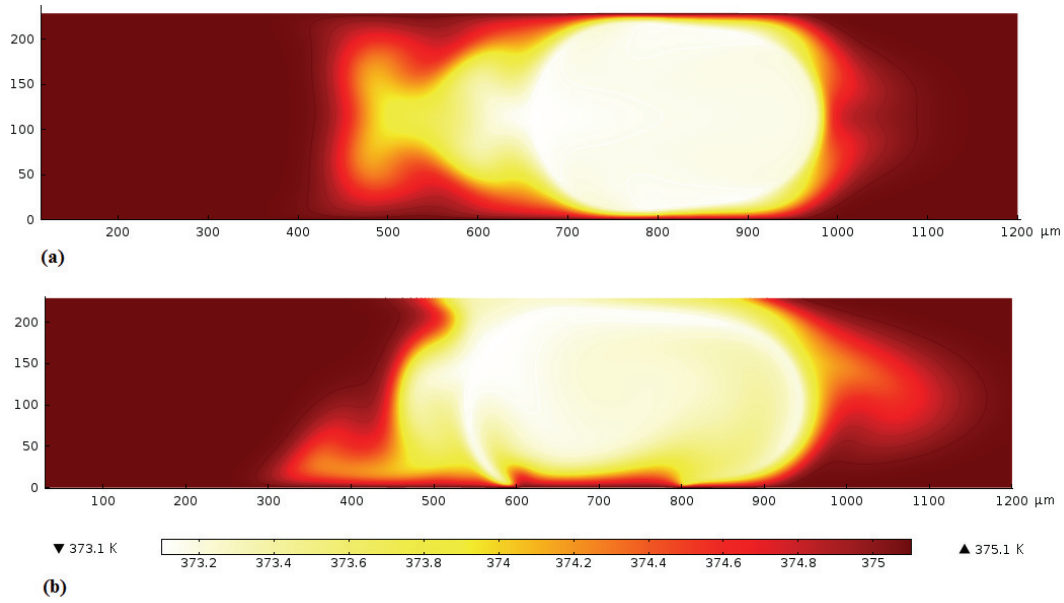

Figure 8. The temperature distribution inside and around the elongated vapor bubble (a) XY plane and (b) ZY plane at t = 1.8 ms.

Figures 8 a, b illustrate the temperature distribution inside and around the elongated vapor bubble in the central horizontal XY plane and the central vertical ZY plane, respectively. Figure 8a shows that the temperature inside the bubble remains at the saturation temperature due to the thin saturated liquid film between the bubble and the side walls. As the bubble evolves into an elongated one, the temperature gradient increases in the thermal boundary layer developed on the side walls. This increases the local heat flux as well. Figure 8b indicates that the adiabatic top wall remains at the saturation temperature where it meets the elongated vapor bubble. On the other hand, the part of the bubble touching the bottom wall is at the superheated temperature.

Figure 9a demonstrates the local heat transfer coefficient and the heat flux along the side wall of the microchannel. It is observed that the evaporation heat transfer coefficient increases to 91200 $W/m^2 \cdot K$ at L = 700 µm, where the thickness of the thin liquid layer between the bubble and the wall is the smallest. The corresponding maximum heat flux is 182 kW/m^2.

Figure 9b shows the local heat transfer coefficient and the heat flux along the bottom wall of the microchannel where the nucleated vapor bubble lies on it. The local heat transfer coefficient increases up to around 137 000 $W/m^2 \cdot K$ at locations where the liquid film, the bubble and the wall are all in contact. When the bubble touches the bottom wall on the other hand, the heat transfer coefficient drops significantly due to diminishing temperature gradients. It can be observed from Figure 8b that a maximum heat flux of 270 KW/m^2 could be dissipated from the bottom wall. The average heat transfer coefficients of the bottom and side walls are illustrated in Figure 10. Since the bubble nucleates on the bottom wall initially, the heat transfer coefficient at the bottom wall is not zero at the initial time. At about 1 ms the bubble starts to elongate and the average heat transfer increases linearly.

Figures 11 a, b display the pressure inside and around the elongated vapor bubble at the central XY and ZY planes. The pressure inside the bubble is 101.95 kPa which is about 450 Pa higher than that of the liquid around it. The mass flux leaving the liquid surface leads to the increase in the vapor pressure, and to the expansion of the vapor region. The difference between the downstream and upstream pressures is about 100 Pa. At the interface, especially around the nose of the bubble, higher pressure gradients exist, which is a similar trend to that observed in the velocity plots of Figure 7. The presence of the surface tension force leads to this discontinuity in pressure across the interface.

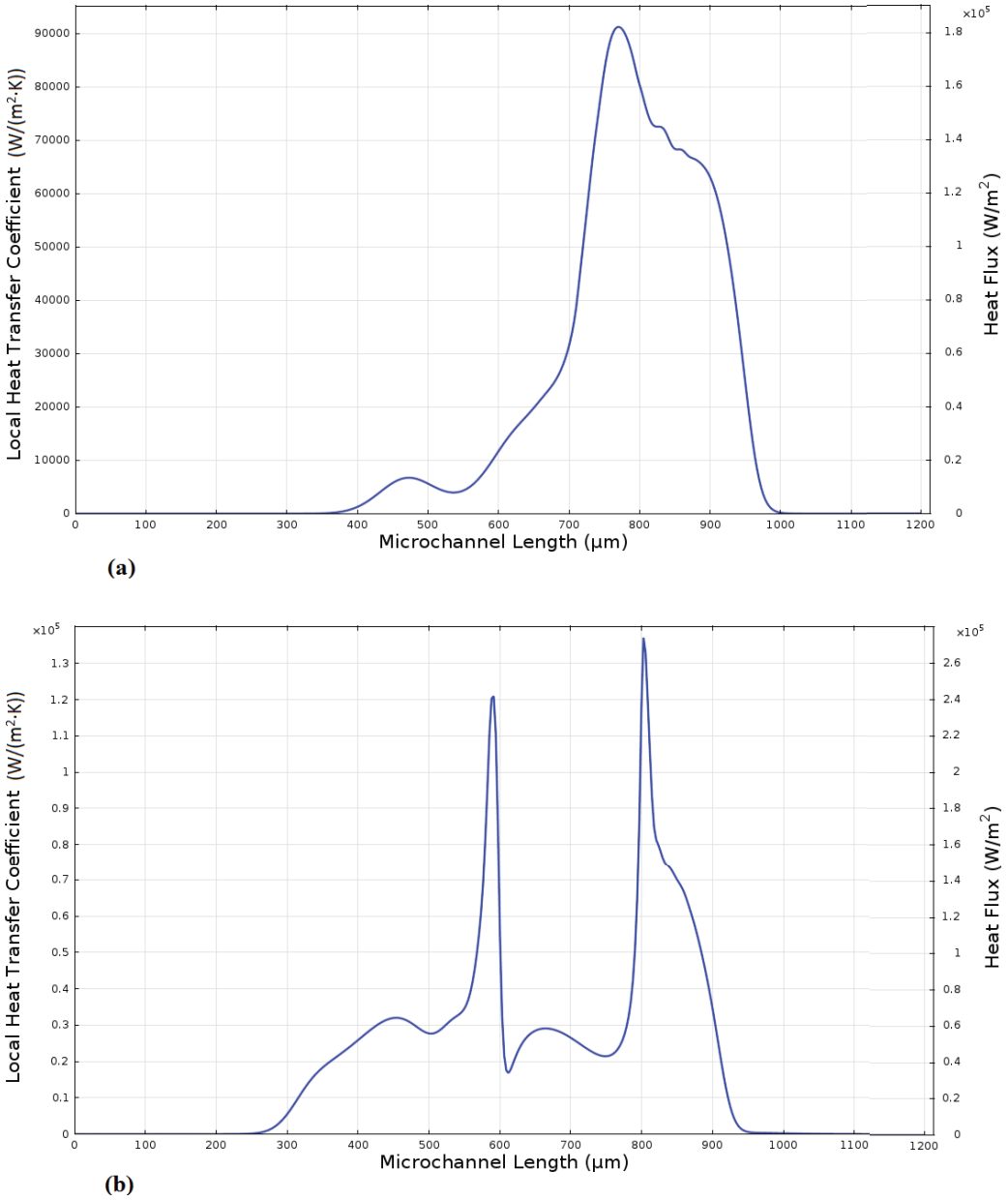

Figure 9. The local heat transfer coefficient and the heat flux on (a) the bottom wall and (b) the side wall at t = 1.8 ms.

To investigate the influence of the contact angle on the bubble shape, and eventually on the heat transfer performance, four different contact angles, namely, 20°, 30°, 40° and 80° have been considered. The respective simulations have been conducted at various inlet velocities of 0.0645 m/s (Re = 50), 0.129 m/s (Re = 100), and 0.258 m/s (Re = 200) in order to include the simultaneous effects of the inlet velocity and the contact angle. Figures 12-14 compare the average heat transfer coefficient over the bottom wall as a function of time for different contact angles.

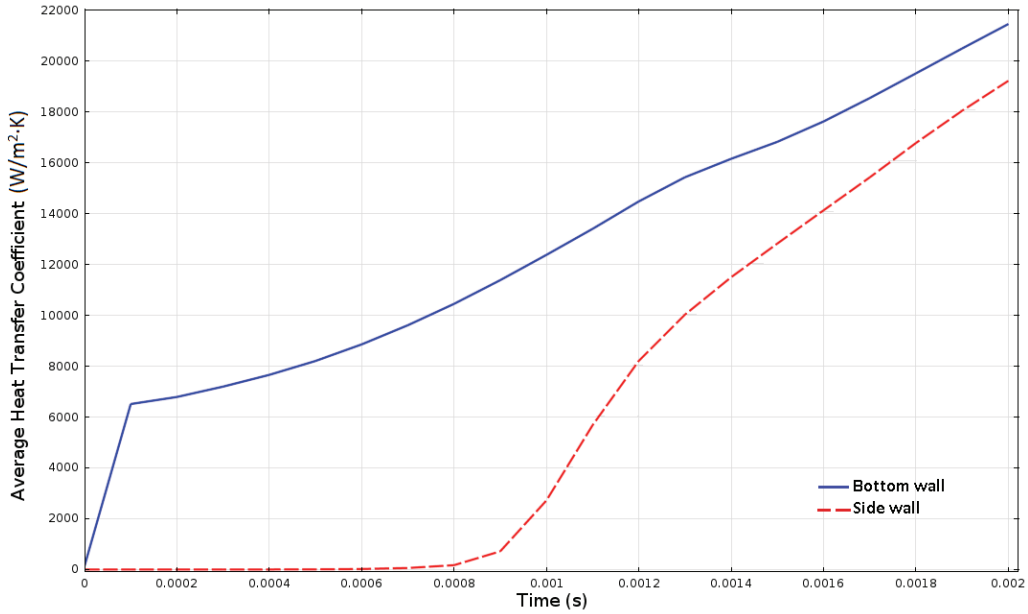

Figure 10. The average heat transfer coefficients over the side walls and the bottom wall.

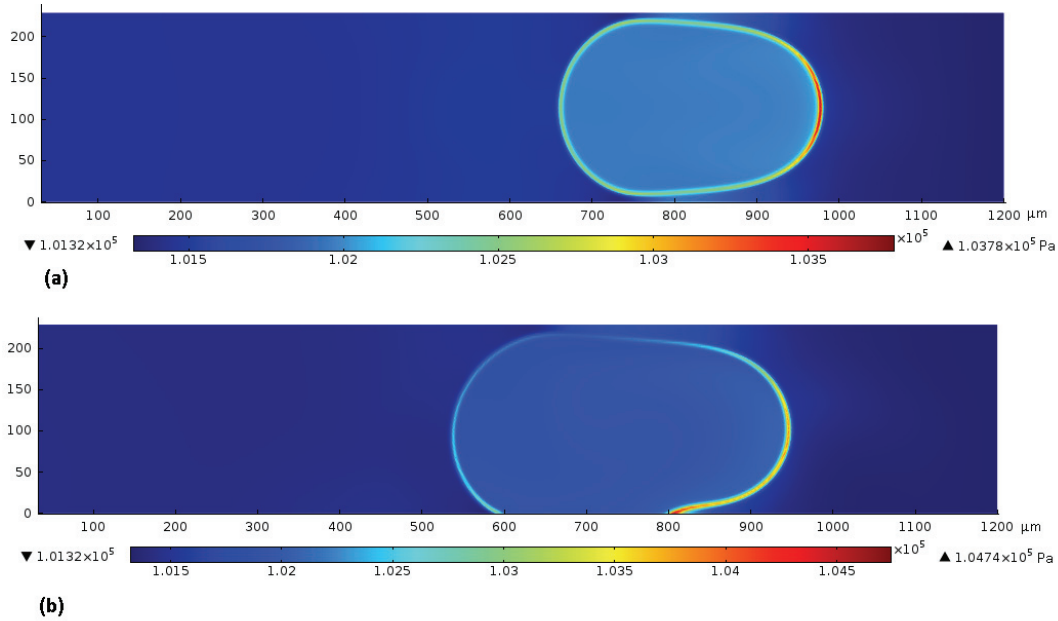

Figure 11. The pressure distributions of the central XY plane (a) and the central ZY plane (b) at t = 1.8 ms.

Figure 12 illustrates that at the lowest inlet velocity of 0.0645 m/s, the heat transfer coefficient gradually increases with time for the contact angles of $\theta = 30^\circ$, 40° and 80°. For $\theta = 20^\circ$, on the other hand, the average heat transfer coefficient fluctuates with time. The reason may be that the bubble cannot stay attached to the bottom wall as it elongates along the microchannel length due to the low contact angle. This behavior is also observed at higher inlet velocities.

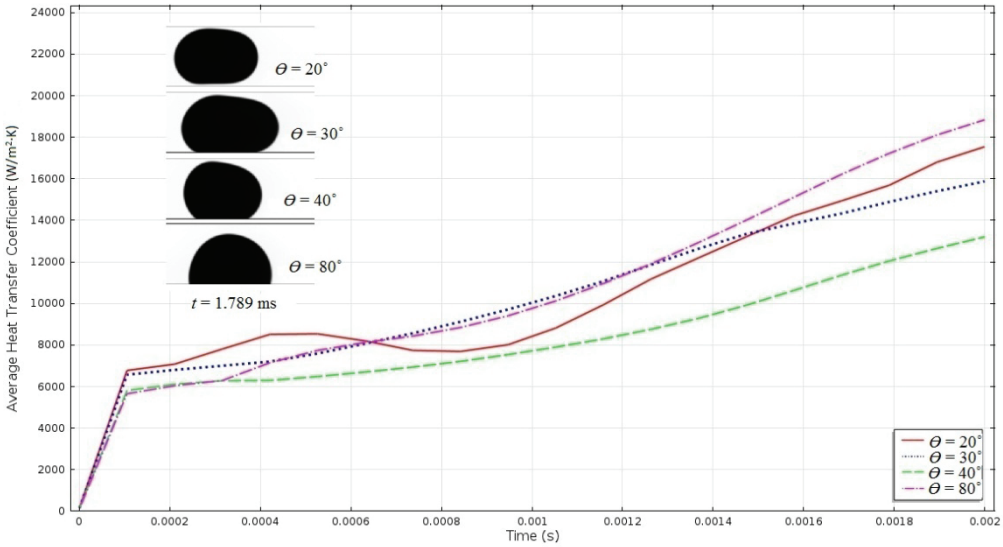

Figure 12. The effect of the contact angle on the average heat transfer coefficient for the inlet velocity of 0.0645 m/s.

When the inlet velocity is doubled as demonstrated in Figure 13, the average heat transfer coefficient also increases for all contact angles. For $\theta = 30^{\circ}$, the amount of the thin liquid layer between the wall and the bubble nose increases with increased velocity. It is for this reason that the heat transfer coefficient is the highest for $\theta = 30^{\circ}$ and keeps increasing with increased inlet velocity as shown in Figure 14. For all velocities, the bubble is elongated the most for $\theta = 30^{\circ}$. The increased evaporation surface area of the longer bubble also supports the increased heat transfer rate.

As the inlet velocity is further increased, as illustrated in Figure 14, the heat transfer coefficient increases sharply for the lower contact angles of $\theta = 20^{\circ}$ and $\theta = 30^{\circ}$. On the other hand, the increase is more gradual, and relatively lower heat transfer coefficients are attained for $\theta = 40^{\circ}$ and $\theta = 80^{\circ}$.

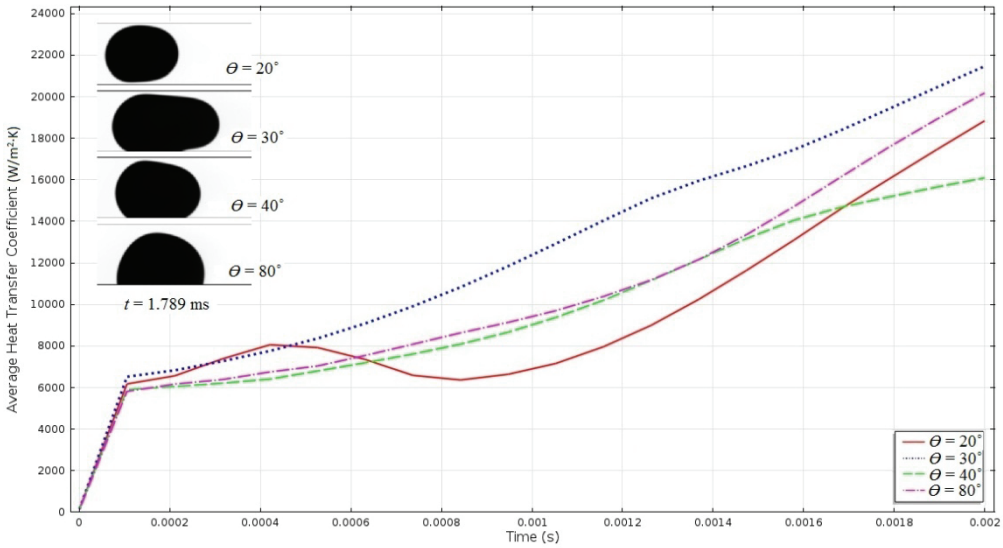

Figure 13. The effect of the contact angle on the average heat transfer coefficient for the inlet velocity of 0.129 m/s.

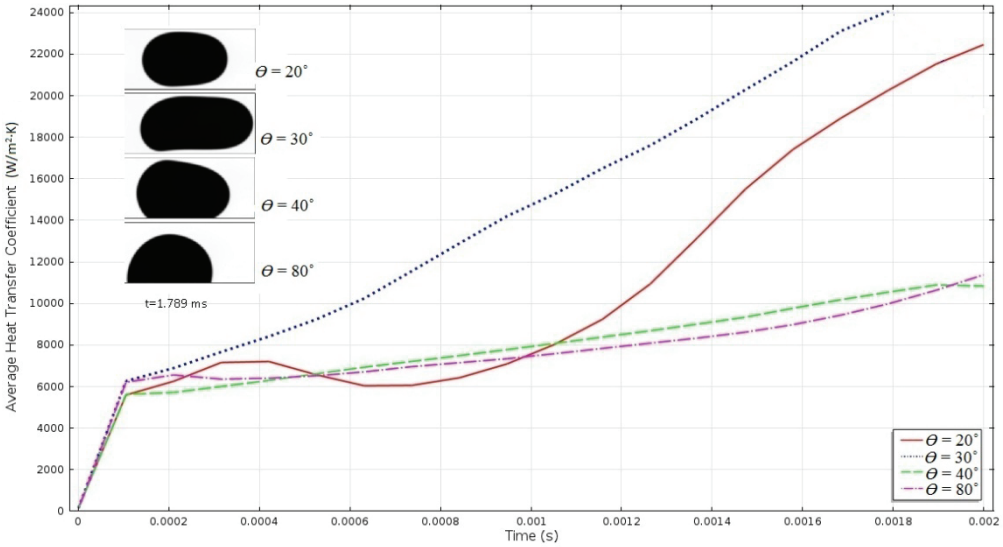

Figure 14. The effect of the contact angle on the average heat transfer coefficient for inlet velocity of 0.258 m/s.

4. CONCLUSIONS

A numerical model based on the phase-field method has been developed, for the first time in the literature, to investigate the hydrodynamics and heat transfer characteristics of a vaporized elongated bubble in a rectangular microchannel. In the simulations, an initially nucleated bubble comes in contact with superheated water and starts growing. The simulated vapor bubble shape and the growth rate are in very good agreement with experimental results available in the literature. With the developed model, it is possible to accurately estimate the velocity, temperature and pressure fields inside the microchannel at any desired time, which is rather a difficult task in an experimental study.

The variations of the local heat transfer coefficient and the heat flux along the microchannel have been investigated as well. In addition, the effects of the contact angle, and water inlet velocity on the average heat transfer coefficient have been demonstrated. A maximum local heat transfer coefficient of 137000 W/m^2·K has been attained at locations where the liquid film, the bubble and the wall are all in contact. A maximum heat flux of 270 kW/m^2 could be dissipated from the bottom wall.

Since the simulation of two-phase flow with evaporation in microchannels is mesh dependent and time consuming, the 2D simulation by using of Cahn-Hilliard phase-field method yields accurate results reducing the need for a 3D analysis.

This method could be further extended to investigate the hydrodynamics and heat removal performance of the slug flow, annular flow, and the impact of parameters such as the surface roughness of the microchannels. An adaptive mesh refinement technique may also be employed at the thin bubble interface to improve the accuracy at the cost of increased running time.

ACKNOWLEDGEMENTS

This project is supported by the Scientific and Technological Research Council of Turkey (TÜBİTAK) under grant number 112M168.

REFERENCES

[1] J.R. Thome, Boiling in microchannels: a review of experiment and theory, *Int. J Heat Fluid Flow* 25, 2004, 128–139.

[2] Z. Guo, D. F. Fletcher, B. S. Haynes, A Review of Computational Modelling of Flow Boiling in Microchannels , *J. Comput. Multiphase Flows*, 2014, 79-110.

[3] V. Talimi, Y.S. Muzychka, S. Kocabiyik, A review on numerical studies of slug flow hydrodynamics and heat transfer in microtubes and microchannels, *Int. J. Multiphase Flow* 39, 2012, 88–104.

[4] S. Saisorn, S. Wongwises, A critical review of recent investigations on flow pattern and heat transfer during flow boiling in micro-channels, *Frontiers in Heat and Mass Transfer* (FHMT) 3, 2012, 013006-1-15.

[5] L. Cheng, Fundamental Issues of Critical Heat Flux Phenomena During Flow Boiling in Microscale-Channels and Nucleate Pool Boiling in Confined Spaces, *Heat Transfer Eng*. 34(13), 2013, 1016–1043.

[6] B. Agostini, M. Fabbri, J.E. Park, L. Wojtan, J.R. Thome, B. Michel, State of the art of high heat flux cooling technologies, *Heat Transfer Eng*. 28, 2007, 258–281.

[7] Y.Q. Zu, Y.Y. Yan, S. Gedupudi, T. G. Karayiannis, D.B.R. Kenning, Confined bubble growth during flow boiling in mini-micro-channel of rectangular cross-section part II: approximate 3-D numerical simulation, *Int. J. Therm. Sci*. 50, 2011, 267-273.

[8] Z. Dong, J. Xu, F. Jiang, P. Liu, Numerical study of vapor bubble effect on flow and heat transfer in microchannel, *Int. J. Therm. Sci*. 54, 2012, 22-32.

[9] D.L. Sun, J.L. Xu, L. Wang, Development of a vapor-liquid phase change model for volume-of-fluid method in FLUENT, *Int. Comm. Heat Mass Transf*. 39, 2012, 1101-1106.

[10] M. Magnini, B. Pulvirenti, J.R. Thome, Numerical investigation of hydrodynamics and heat transfer of elongated bubbles during flow boiling in a microchannel, *Int. J. Heat Mass transfer* 59, 2013, 451-471.

[11] L. Consolini, J.R. Thome, A heat transfer model for evaporation of coalescing bubbles in micro-channel flow, *Int. J. Heat Mass Transfer* 31, 2010, 115-125.

[12] A. Mukherjee, S.G. Kandlikar, Z.J. Edel, Numerical study of bubble growth and wall heat transfer during flow boiling in a microchannel, *Int. J. Heat Mass Transfer* 54, 2011, 3702-3718.

[13] R. Jafari, T. Okutucu-Ozyurt, 3D Numerical Modeling of Boiling In a Microchannel by Arbitrary Lagrangian-Eulerian (ALE) Method, *Appl. Math. Comput*., 2015, DOI: 10.1016/j.amc.2015.03.042.

[14] S. Zhou, X. Xu, B.G. Sammakia, Modeling of boiling flow in microchannels for nucleation characteristics and performance optimization, *Int. J. Heat Mass Transfer* 64, 2013, 706–718.

[15] H.A. Akhlaghi Amiri, A.A. Hamouda, Evaluation of level set and phase-field methods in modeling two phase flow with viscosity contrast through dual-permeability porous medium, *Int. J. Multiphase Flow* 52, 2013, 22–34.

[16] P. Yue, C. Zhou, J.J. Feng, C.F. Ollivier-Gooch, H.H. Hu, Phase-field simulations of interfacial dynamics in viscoelastic fluids using finite elements with adaptive meshing, *J. Comput. Phys*. 219, 2006, 47–67.

[17] D.M. Anderson, G.B. McFadden, Diffuse-interface methods in fluid mechanics, *Annu. Rev. Fluid Mech*. 30, 1998, 139–165.

[18] C. Liu, J. Shen, A phase-field model for the mixture of two incompressible fluids and its approximation by a Fourier-spectral method, *Physica D* 179, 2003, 211–228.

[19] P. Yue, J.J. Feng, C. Liu, J. Shen, A diffuse-interface method for simulating two-phase flows of complex fluids, *J. Fluid Mech*. 515, 2004, 293–317.

[20] H. Gomez, V.M. Calo, Y. Bazilevs, T. J.R. Hughes, Isogeometric analysis of the Cahn-Hilliard phase-field model, Comput. Methods Appl. *Mech. Engrg*. 197, 2008, 4333–4352.

[21] I. Steinbach, Phase-field models in materials science, Modelling Simul. Mater. *Sci. Eng*. 17, 2009, 073001-1-31.

[22] C. Miehe, F. Welschinger, M. Hofacker, Thermodynamically consistent phase-field models of fracture: variational principles and multi-field FE implementations, *Int. J. Numer. Meth. Engng* 83, 2010, 1273–1311.

[23] D. Jacqmin, Calculation of two-phase Navier–Stokes flows using phase-field modeling, *J. Comput. Phys*. 155,1999, 96–127.

[24] H. D. Ceniceros, R. L. Nós, A. M. Romac, Three-dimensional, fully adaptive simulations of phase-field fluid models, *J. Comput. Phys*. 229, 2010, 6135–6155.

[25] V.E. Badalassi, H.D. Ceniceros, S. Banerjee, Computation of multiphase systems with phase field models, *J. Comput. Phys*. 190, 2003, 371–397.

[26] A. Badillo, Quantitative phase-field modeling for boiling phenomena, *Phys. Rev*. E 86, 2012, 041603-1-25.

[27] W.H. Lee, A pressure iteration scheme for two-phase flow modeling, T.N. Veziroglu (Ed.), Multiphase Transport Fundamentals, Reactor Safety, *Applications*, vol. 1, Hemisphere Publishing, Washington, DC, 1980.

[28] Z. Yang, X.F. Peng, P. Ye, Numerical and Experimental Investigation of Two Phase Flow During Boiling in a Coiled Tube, *Int. J. Heat Mass Transfer* 51, 2008, 1003-1016.